



www.advenergymat.de

Approaching the Minimum Thermal Conductivity in Rhenium-Substituted Higher Manganese Silicides

Xi Chen, Steven N. Girard, Fei Meng, Edgar Lara-Curzio, Song Jin, John B. Goodenough, Iianshi Zhou, and Li Shi*

Higher manganese silicides (HMS) made of earth-abundant and non-toxic elements are regarded as promising p-type thermoelectric materials because their complex crystal structure results in low lattice thermal conductivity. It is shown here that the already low thermal conductivity of HMS can be reduced further to approach the minimum thermal conductivity via partial substitution of Mn with heavier rhenium (Re) to increase point defect scattering. The solubility limit of Re in the obtained $Re_xMn_{1-x}Si_{1.8}$ is determined to be about x = 0.18. Elemental inhomogeneity and the formation of ReSi_{1.75} inclusions with 50-200 nm size are found within the HMS matrix. It is found that the power factor does not change markedly at low Re content of $x \le 0.04$ before it drops considerably at higher Re contents. Compared to pure HMS, the reduced lattice thermal conductivity in Re_xMn_{1-x}Si_{1.8} results in a 25% increase of the peak figure of merit ZT to reach 0.57 \pm 0.08 at 800 K for x = 0.04. The suppressed thermal conductivity in the pure Re_xMn_{1-x}Si_{1.8} can enable further investigations of the ZT limit of this system by exploring different impurity doping strategies to optimize the carrier concentration and power factor.

1. Introduction

Thermoelectric (TE) materials, which can convert temperature gradients directly into electricity and vice versa, have received renewed interest for waste heat recovery and refrigeration applications. The conversion efficiency of a TE material is determined by the dimensionless figure of merit $ZT = S^2 \sigma T / (\kappa_E + \kappa_L)$, where S, σ , κ_E , κ_L , and T represent the Seebeck coefficient, electrical conductivity, electronic thermal conductivity,

X. Chen, Prof. J. B. Goodenough,
Prof. J. S. Zhou, Prof. L. Shi
Materials Science and Engineering Program
Texas Materials Institute
The University of Texas at Austin
Austin, TX 78712, USA
E-mail: lishi@mail.utexas.edu
Dr. S. N. Girard, F. Meng, Prof. S. Jin
Department of Chemistry
University of Wisconsin – Madison

Madison, WI 53706, USA
Dr. E. Lara-Curzio
Materials Science and Technology Division

Oak Ridge National Laboratory 1 Bethel Valley Road Oak Ridge, TN 37831, USA

DOI: 10.1002/aenm.201400452



lattice thermal conductivity, and absolute temperature, respectively. Recent efforts to raise the ZT of TE materials have relied on several strategies: reduction of the lattice thermal conductivity by nanostructuring^[3–7] and alloy scattering,^[8,9] optimization of the power factor ($PF = S^2$ σ) by tuning the carrier concentration,^[10–12] enhancement of the Seebeck coefficient by band engineering,^[13–15] and employment of complex crystal structures that possess intrinsically lower lattice thermal conductivity.^[16,17]

Higher manganese silicides (HMS, or $MnSi_{\approx 1.75}$) are regarded as promising p-type TE materials because they are comprised of inexpensive and nontoxic elements and exhibit good chemical stability at high temperatures. The complex crystal structure of these homologous HMS compounds consists of a Mn sublattice and an interpenetrating helical Si

sublattice, characteristic of the Nowotny chimney ladder (NCL) phases. Single-crystal structures of several closely related HMS phases, e.g., $\rm Mn_4Si_7,^{[18]}~Mn_{11}Si_{19},^{[19]}~Mn_{15}Si_{26},^{[20]}~Mn_{19}Si_{33},^{[21]}$ and $\rm Mn_{27}Si_{47},^{[22]}$ have been reported. These phases have similar a and b lattice parameters arising from the Mn sublattice, but a large c lattice parameter that varies from 17.5 Å for $\rm Mn_4Si_7$ to 117.9 Å for $\rm Mn_{27}Si_{47}$ and is dependent on the Si sublattice. The complexity of the NCL structure gives rise to anisotropic TE properties and intrinsically low thermal conductivity. The thermal conductivity along the c axis and a axis of HMS crystals are reported to be about 2 W m $^{-1}$ K $^{-1}$ and 4 W m $^{-1}$ K $^{-1}$ at 300 K, respectively. $^{[23]}$

To date, most of the investigations of HMS and related compounds have been focused on optimizing the electrical transport properties of HMS by chemical substitution [24–30] and suppressing the lattice thermal conductivity by nanostructuring. [21,31–34] Relatively high ZT values of 0.6–0.7 have been achieved in HMS synthesized by various methods, [23,25,27,28,31] such as Ge-doped HMS prepared by induction melting and hot-pressing, [25] undoped HMS with in situ nanoscale MnSi prepared by spin-melting and spark plasma sintering (SPS), [31] and complex doped HMS single crystals prepared by the Bridgman method. [23,35] Previously, we have investigated the effects of Al and Ge co-doping on the TE properties of HMS. [36] The peak power factor was found at a hole concentration between 1.8×10^{21} and 2.2×10^{21} cm⁻³, and the maximum



ZT value of 0.57 was achieved at 823 K for the compositions $Mn(Al_{0.0045}Si_{0.9955})_{1.8}$ and $Mn(Al_{0.0035}Ge_{0.015}Si_{0.9815})_{1.8}$.

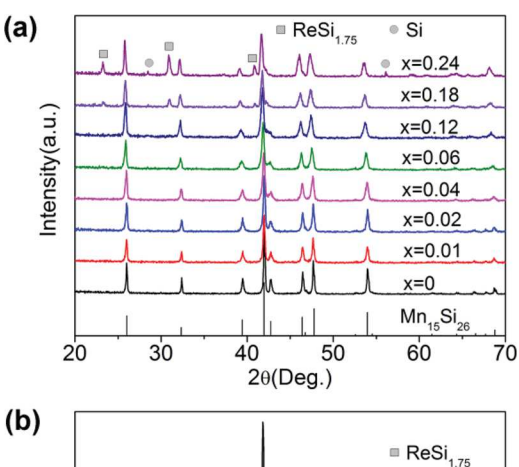
Partial substitution of elements with heavy atoms can reduce the lattice thermal conductivity due to increased alloy scattering resulting from the mass and strain fluctuations. [9,37] This approach has been explored in several recent experimental works on $\mathrm{Mn_{1-x-y}Cr_xRu_ySi_{1.74}}$, [27] $\mathrm{Mn_{0.9}Ru_{0.1}Si_y}$ [30] and an rhenium (Re)-substituted HMS sample with an unspecified Re content. [38] Despite the observed reduced thermal conductivity in the reported Re-substituted HMS sample, [38] critical questions remain on the solubility limit of Re in HMS, the correlations between the Re content, the power factor, and lattice thermal conductivity, and most importantly, the extent that the lattice thermal conductivity can be reduced in comparison to the theoretical minimum thermal conductivity of HMS.

Here, we report the findings from a systematic study of the structure-TE property relationship of Re_xMn_{1-x}Si_{1.8} (x = 0-0.24), which were prepared by solid-state reaction (SSR) followed by ball-milling (BM) and spark plasma sintering (SPS). In conjunction with the experimental results, theoretical analysis is used to develop a better understanding of the effects of heavy-element substitution on the TE properties. It is found that the solubility of Re in HMS is less than x = 0.18. The lattice thermal conductivity for Re_{0.12}Mn_{0.88}Si_{1.8} is effectively suppressed due to increased alloy scattering of phonons to be about 30% lower at 723 K than that of pure HMS samples prepared by the same method. The minimum thermal conductivity model^[39] is used to determine that the reduced lattice thermal conductivity has approached the theoretical minimum of Re-substituted HMS. In comparison, the power factor is not affected by the Re substitution at $x \le 0.04$. These results already lead to a 25% ZT increase in pure $Re_xMn_{1-x}Si_{1.8}$ with x = 0.04compared to pure HMS, and may enable further efforts to increase the ZT of Re-substituted HMS by exploring additional impurity doping to optimize the carrier concentration.

2. Results and Discussion

2.1. Phase and Microstructures

Figure 1a shows the X-ray diffraction (XRD) patterns of the bulk samples obtained after SPS. It can be seen that Re readily substitutes for Mn to obtain $Re_xMn_{1-x}Si_{1.8}$ for $x \le 0.12$. Diffraction peaks from Si and ReSi_{1.75} can be discerned in the samples with higher Re concentrations ($x \ge 0.18$). However, high-resolution synchrotron XRD performed on the sample with x = 0.06(Figure 1b) reveals that the second phase ReSi_{1.75} is formed even in the samples with low Re concentrations. With increasing Re concentration, the diffraction peaks from HMS become increasingly broad. As discussed below, such broadening is attributed to locally inhomogeneous compositions in the material. In addition, the intensity of the (11 γ) peak at $2\theta = 42.8^{\circ}$ decreases with increasing Re content, where γ is the number of Si atoms in the formula of different HMS phases. It has similarly been reported that the intensity and position of this peak are sensitive to the doping concentration in Ge-doped HMS.[25] The HMS powders synthesized are usually a mixture of several HMS phases with different c lattice parameters rather than a



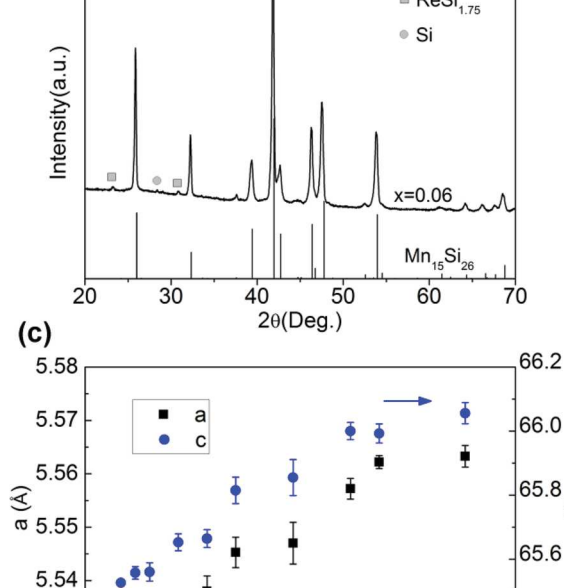


Figure 1. a) The XRD patterns of various $Re_xMn_{1-x}Si_{1.8}$ samples after SPS. b) High resolution synchrotron XRD of the $Re_{0.06}Mn_{0.94}Si_{1.8}$ sample. c) The measured mean lattice parameters of $Re_xMn_{1-x}Si_{1.8}$ as a function of x.

0.15

0.20

0.10

pure single HMS phase.^[40] Because of this, the lattice parameters of all samples were calculated from the XRD peak positions on the premise that the material was an average phase of Mn₁₅Si₂₆. It should be noted that the as-obtained lattice parameters are the mean values of a locally inhomogeneous material.^[29] Both a and c lattice parameters increase monotonically up to x = 0.18 as shown in Figure 1c, which is due to the larger metallic radius of Re $(r_{\rm Re} = 1.37 \text{ Å})$ as compared to that of Mn $(r_{\rm Mn} = 1.27 \text{ Å})$.^[41] Since the mean lattice parameters no longer change as the Re concentration is increased beyond x = 0.18, as is shown in Figure 1c, it can be concluded that the solubility limit of Re in HMS is reached according to Vegard's law.

Figure 2 shows the microstructure of the bulk samples prepared by SPS. In Figure 2a,b, the comparison of scanning electron microscope (SEM) images of pure HMS with

5.53

5.52

0.00

0.05

65.4

65.2

www.advenergymat.de

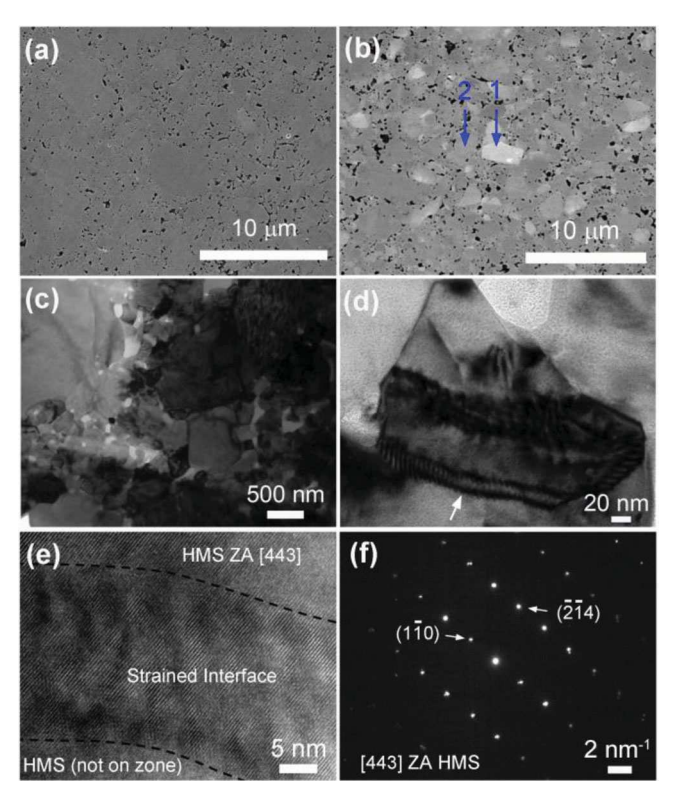


Figure 2. SEM images of a) the pure HMS and b) the $Re_{0.04}Mn_{0.96}Si_{1.8}$ sample after SPS. The blue arrows in (b) point to the regions where the EDS analysis was performed. c,d) Zero-beam bright-field TEM images of the $Re_{0.04}Mn_{0.96}Si_{1.8}$ sample. The white arrow in (d) points to the strain locations. e) High-resolution TEM of the $Re_{0.04}Mn_{0.96}Si_{1.8}$ sample. f) The selected area electron diffraction of (e) obtained along the [443] zone axis (ZA). The SAED pattern was indexed based on the structure of the simplest HMS phase, Mn_4Si_7 .

Re-substituted HMS (x = 0.04) reveals an increased compositional inhomogeneity in the Re-substituted HMS samples as evidenced by differences in contrast resulting primarily from the incorporation of Re. Energy-dispersive X-ray spectroscopy (EDS) analysis reveals that the contrast differences are related to a compositional variation. The atomic ratio in region 1 (bright area) of Figure 2b contains a higher concentration of Re, with the atomic ratio between Re, Mn, and Si being Re:Mn:Si = 7:22:71, whereas the composition of the region 2 (dark area) of Figure 2b is relatively Re deficient, Re:Mn:Si = 2:31:67. Analysis of multiple grains reveals that the Re substitution is essentially the same within a grain, but that the Re concentration can vary considerably between grains. As a result, the observed broadening of the XRD peaks with increasing Re incorporation (Figure 1a) has been attributed to the inhomogeneous distribution of Re within the collection of HMS grains in the SPS samples. It should be noted that such inhomogeneous distribution of substitution elements has also been observed in several other doped NCL phases, such as $Ru_{1-x}Re_xSi_v^{[42]}Mn_{1-x}Cr_xSi_{1.7}^{[29]}$ and $Ru_{1-x}Mn_xSi_v$ [30]

To better understand the microstructure, the Re-substituted sample with x=0.04 was examined with transmission electron microscopy (TEM), Figure 2c–f. Figure 2c is a typical low-magnification TEM image of the sample. The sample exhibits

a broad particle size distribution, ranging from about 50 nm to about 5 µm. The highly energetic process of ball milling and SPS introduces considerable strain on the surface of the HMS grains, which become randomly distributed throughout the sample (Figure 2c). Strain is alleviated at the interfaces between HMS grains by regularly spaced dislocations, as shown in the strain fields around the particle in Figure 2d,e. Figure 2e shows the interface between two HMS grains and strain dislocations at higher resolution. The top portion of the sample is along the [443] zone axis of HMS, shown in the selected-area electron diffraction (SAED) in Figure 2f. The total thickness of the interfacial strain-field region between HMS grains is observed to be about 25 nm. The adjacent HMS grain, shown at the bottom of the image in Figure 2e, lies on a different crystallographic zone axis, resulting in a loss of lattice contrast at the bottom of the image.

ReSi_{1.75} particles with size generally in the range of 50–200 nm can be observed to be dispersed within the matrix of samples with x as low as 0.04 (Figure 3), in agreement with high-resolution XRD results indicating that while Re does alloy with HMS, there also exists some phase immiscibility that produces small inclusions of ReSi_{1.75}. The larger ReSi_{1.75} particles observed in Figure 3a,b are randomly oriented with respect to each other and the HMS matrix. Smaller ReSi_{1.75} particles with size less than about 50 nm show improved alignment within the HMS matrix, evidenced by lattice contrast observed along the same zone in the ReSi_{1.75} particle as in the HMS matrix, Figure 3c,d. The coherency and epitaxy of the ReSi_{1.75} cannot be determined, resulting from the completely random orientations of the grains from sample preparation and the

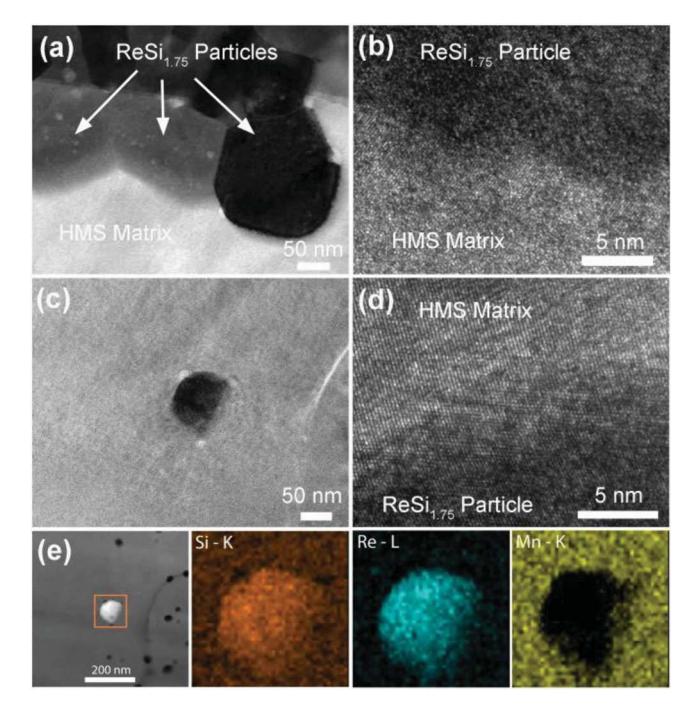


Figure 3. a) TEM image of Re_{0.04}Mn_{0.96}Si_{1.8} showing the embedded ReSi_{1.75} nanoparticles. b) The high-resolution TEM of the interface between ReSi_{1.75} and HMS. c) TEM image of an embedded ReSi_{1.75} nanoparticle. d) The high-resolution TEM of the interface between ReSi_{1.75} and HMS. e) Elemental maps of ReSi_{1.75} nanoparticle.

www.MaterialsViews.com

relatively small area afforded by the focused ion beam (FIB) preparation of the TEM sample. EDS spectra confirm that the small inclusions are rich in Re and deficient in Mn, according to Figure 3e.

2.2. Electronic Transport Properties

Hall coefficient measurements were carried out for the Resubstituted samples. As shown in Figure 4a, the measured room-temperature hole concentration (p) appears to increase slightly with Re substitution, although the difference is comparable to the measurement uncertainty. Since Re is isoelectronic with Mn, the increase of p is unexpected. Several first-principles calculations^[43] indicate that the band structure of HMS strongly depends on the atomic arrangement and the existence of stacking faults. Recently, Allam et al.[44] found that the density of states (DOS) of HMS changes by Re substitution according to a first-principles calculation. Moreover, Zhou et al. [25] reported that the hole concentration was increased in Ge-doped HMS even though Ge is isoelectronic with Si. They found that Ge substitution can disturb the arrangement of the Si subcells and possibly form stacking faults in the HMS. Thus, Re substitution is likely to alter the band structure and possibly the Fermi level or DOS near the Fermi level, potentially increasing the hole concentration. It should also be noted that the formation of defects at a higher concentration of Re could also change the hole concentration of HMS. However, detailed first-principles calculation

is needed to better understand the cause of the increased hole concentration in Re-substituted HMS. In addition, Figure 4c shows that the hole concentration is essentially independent of temperature for the samples with x=0, 0.04 and 0.12. This feature is characteristic of a degenerate p-type semiconductor.

As shown in Figure 4b, the room-temperature mobility ($\mu_{\rm H}$) of Re-substituted samples decreases with the increase of Re content, which can be attributed to enhanced alloy scattering. In comparison, carrier scattering by ReSi_{1.75} particles is not considered to be important here because the carrier mean free path of HMS is reported to be about several nm,^[32] which is much smaller than the size or interparticle spacing of ReSi_{1.75} particles. Alloy scattering adds a neutral impurity scattering term ($\mu_{\rm alloy}$) to the ionized impurity and phonon scattering. Thus, the total mobility (μ) is given by^[45]

$$\frac{1}{\mu} = \frac{1}{\mu_{\rm o}} + \frac{1}{\mu_{\rm alloy}},\tag{1}$$

where μ_0 is the mobility in pure HMS with x=0 due to scattering by phonons, grain boundary, and ionized impurities, and $\mu_{\rm alloy}$ is the additional alloy scattering in ${\rm Re}_x {\rm Mn}_{1-x} {\rm Si}_{1.8}$, and is proportional to $[f(1-f)]^{-1}$ or $[(x/2.8)(1-x/2.8)]^{-1}$ for ${\rm Re}_x {\rm Mn}_{1-x} {\rm Si}_{1.8}$, where f is the mole fraction of the substitution element in the alloy. [46] By fitting the composition dependence of mobility at room temperature (Figure 4b) with Equation (1), the alloy scattering mobility term at room temperature is determined to be about $\mu_{\rm alloy} = 0.55/[x(1-x/2.8)]$ cm² V⁻¹ s⁻¹.

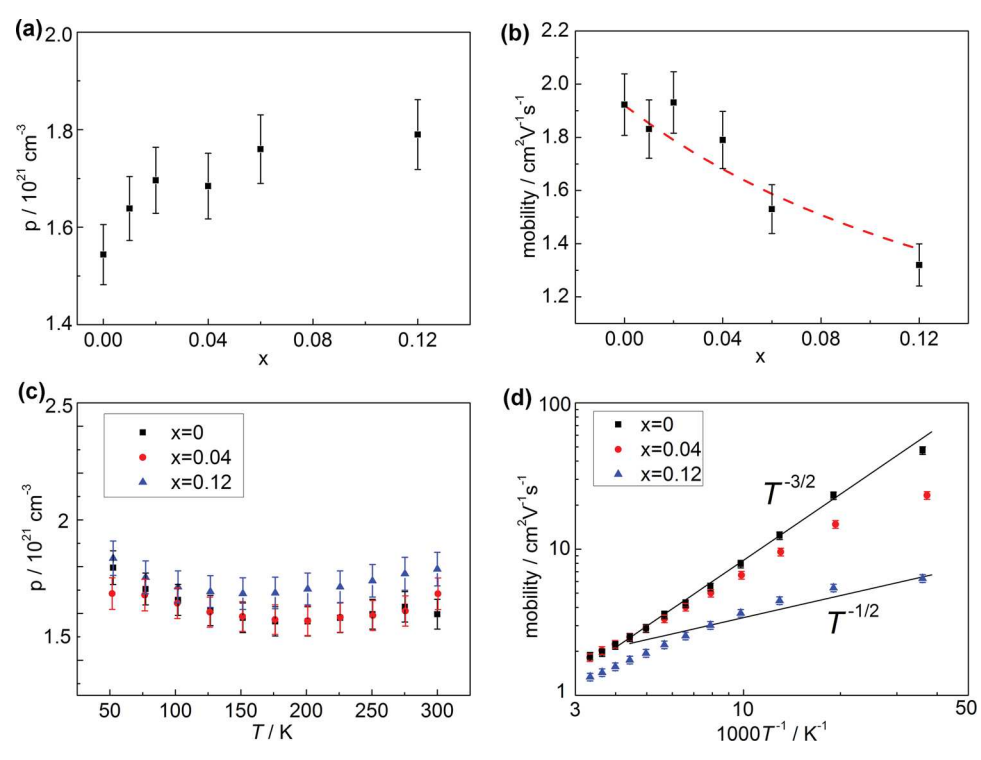


Figure 4. a) Carrier concentration and b) mobility of $Re_xMn_{1-x}Si_{1.8}$ as a function of x at room temperature. c) Carrier concentration and d) mobility of $Re_xMn_{1-x}Si_{1.8}$ with x = 0, 0.04 and 0.12 as a function of temperature. The red dashed line in (b) is the fitting of the measured mobility according to Equation (1).

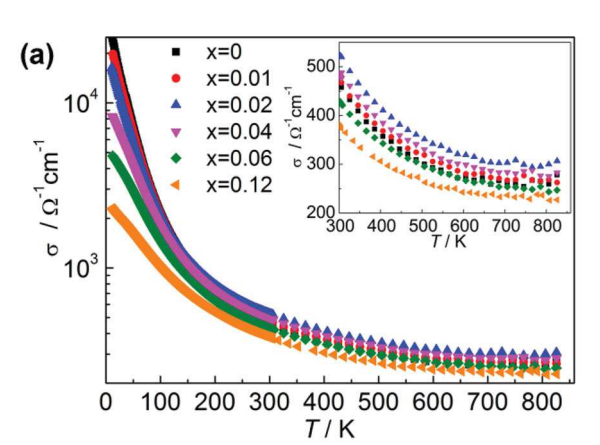
www.advenergymat.de

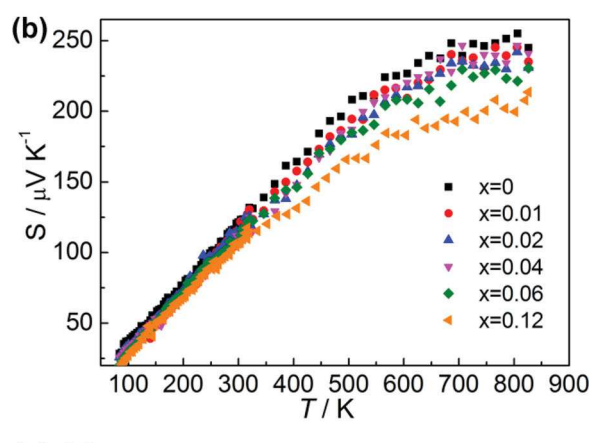
www.MaterialsViews.com

Figure 4d shows the mobility of the Re-substituted samples as a function of temperature. For pure HMS, the mobility $\mu_{\rm H}$ varies approximately as $T^{-3/2}$ for temperatures above 50 K. This result indicates that acoustic phonon scattering^[47] is the dominant carrier scattering mechanism in HMS above 50 K compared to alloy scattering and ionized impurity scattering, which yield $\mu_{\rm H} \propto T^{-1/2[45]}$ and $\mu_{\rm H} \propto T^{3/2,[11,43,45,48]}$ respectively. For the Re-substituted sample with x=0.12, the mobility varies approximately as $T^{-1/2}$ for temperatures below 100 K, suggesting that both phonon scattering and alloy scattering are important in this temperature range. Nevertheless, the mobility of all samples follows the relationship of $\mu_{\rm H} \propto T^{-3/2}$ above 200 K, which suggests that acoustic phonon scattering is dominant at high temperatures.

The temperature dependence of electrical conductivity (σ) and Seebeck coefficient (S) for Re_xMn_{1-x}Si_{1.8} are plotted in Figure 5a,b, respectively. The room-temperature electrical conductivity increases with the Re content from 475 $\Omega^{-1}\mbox{ cm}^{-1}$ in pure HMS to 524 Ω^{-1} cm⁻¹ in the sample with x = 0.02. As the Re content increases further, the room-temperature electrical conductivity decreases. The initial increase of the room-temperature electrical conductivity is caused by the increased carrier concentration (Figure 4a); whereas the decrease of the roomtemperature electrical conductivity at higher Re contents can be attributed to the reduced mobility (Figure 4b). In addition, the electrical conductivity at temperatures below 100 K decreases with Re substitution, which results from enhanced alloy scattering (Figure 4d). The S of all samples decreases monotonically with an increase in the Re content, in agreement with the measured increase in the hole concentration. The power factor (PF) of Re_xMn_{1-x}Si_{1.8} is calculated by using polynomial fits to the measured σ and S and is displayed in Figure 5c. For the samples with $x \le 0.04$, the PF does not change significantly as compared to the pure HMS, which is a consequence of the improved σ and reduced S. However, the samples with higher Re content (x = 0.06 and 0.12) show lower PF than other samples, which is due to the much reduced *S*.

In order to better understand the carrier transport features in Re-substituted HMS, the room-temperature Fermi level ($E_{\rm F}$), hole density of states effective mass (m_h^*) , and Lorenz number (L) are extracted from the measured electrical conductivity, the Seebeck coefficient, and Hall coefficient. These are listed together with other room-temperature properties in Table 1. This analysis is based on a two-band model, where charge carrier scattering is assumed to be dominated by acoustic phonon scattering and grain-boundary scattering. The Lorenz number is calculated from the model as $L = \kappa_E/\sigma T$ at room temperature. The two-band model has been reported in a recent publication. Here, the extracted m_h^* of pure HMS is 9.6 m_o , where m_0 is the free electron mass. This m_h^* value is comparable to the literature values of $12m_0$ reported by Nishida.^[48] In addition, the extracted hole effective mass decreases with the increase of Re content, with the smallest $m_h^* = 8.7 m_o$ found in the sample with x = 0.12. The Fermi level is measured from the conduction band edge and is negative when it is in the band gap or valence band. The Fermi level of pure HMS is 0.81 eV, which is 0.04 eV below the valence band edge as the band gap of HMS is 0.77 eV.[43] The extracted Fermi level decreases slightly as the Re content increases because the measured hole concentration





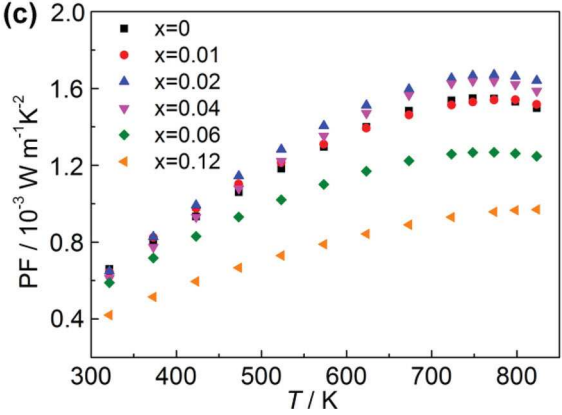


Figure 5. Temperature dependence of transport properties of various $\text{Re}_x \text{Mn}_{1-x} \text{Si}_{1.8}$ samples: a) electrical conductivity with 5% uncertainty, b) Seebeck coefficient with 5% uncertainty, and c) power factor with 11% uncertainty. The inset of (a) is the electrical conductivity in the temperature range of 300 to 850 K.

increases with increasing Re content. The L values were calculated to be in the range from 1.3 to 1.7×10^{-8} V² K⁻², which is lower than the Sommerfeld value of 2.45×10^{-8} V² K⁻² for the metallic limit.

2.3. Thermal Properties and Thermoelectric Figure of Merit

The heat capacity (C_p), thermal diffusivity (α), and total thermal conductivity (κ) for Re_xMn_{1-x}Si_{1.8} are shown in **Figure 6**. The C_p



www.MaterialsViews.com

at 800 K decreases from 0.69 J g^{-1} K⁻¹ in the pure HMS to 0.60 J g⁻¹ K⁻¹ in the sample with x = 0.12. According to the Dulong-Petit Law, the high-temperature limit of heat capacity is $3Nk_B/M$, where N, $k_{\rm B}$ and M are the number of atoms per mole, the Boltzmann constant, and the molar mass of the compound, respectively. Since the atomic mass of Re (186.2 g mol⁻¹) is larger than that of Mn (54.9 g mol⁻¹), the Dulong-Petit limit of Re-substituted HMS should be lower than that of pure HMS, which is consistent with the experimental results. The α of all the samples decreases with increasing Re content. The total thermal conductivity is obtained as $\kappa = \alpha C_p$ ρ , where ρ is the density of the as-prepared samples as shown in Table 1. Although ρ increases with the Re content, the total thermal conductivity was suppressed by Re substitution due to both decreased $C_{\rm p}$ and α . A low κ of 1.7 W m⁻¹ K⁻¹ at 320 K was achieved in the sample with x = 0.12, which is about 30% lower than that of pure HMS prepared with the same method. It is noted that the κ at around 300 K measured by the steady-state method is slightly higher than that obtained by the laser flash diffusivity method. This discrepancy is due to the measurement errors of these two methods. The uncertainties of the steady-state method and the laser flash method are about 15% and 7%, respectively. The larger uncertainty for the steady-state method is caused by radiation losses and heat loss into the thermocouples, which can result in an overestimated thermal conductivity,[11] in addition to the uncertainty in measuring the distance between differential thermocouples used in the measurements.

The lattice thermal conductivity ($\kappa_{\rm I}$) can be obtained by subtracting the electronic thermal conductivity ($\kappa_{\rm F}$) from the total thermal conductivity. For temperatures higher than 300 K, $\kappa_{\rm E}$ is calculated following ref. [36] with the hole, electron, and bi-polar contributions included. For temperatures lower than 300 K, the room-temperature L values listed in Table 1 have been used to calculate $\kappa_{\rm F}$ via Wiedemann-Franz Law $\kappa_{\rm F} = L\sigma T$. The κ_L at 723 K as a function of the Re concentration and κ_L for Re_xMn_{1-x}Si_{1.8} at all measured temperatures are shown in Figure 7a,b, respectively. It is clear that the κ_L is dominant in the HMS samples as compared to $\kappa_{\rm E}$ at temperatures up to 800 K. The $\kappa_{\rm I}$ decreases considerably with increasing Re content over the measured temperature range, indicating that alloying of Re at Mn sites is an effective approach to reducing the κ_L in HMS compounds. The lowest κ_L is obtained for $Re_{0.12}Mn_{0.88}Si_{1.8}$, yielding the value of 1.6 W m⁻¹ K⁻¹ at 723 K, which is about 30% lower than that of pure HMS synthesized with the same method. The reduction of κ_L is mainly due to the point defect scattering for phonons as a result of mass

fluctuations and associated perturbation in the interatomic force constant. In addition, the reduction of κ_L may also have a contribution from the formation of ReSi_{1.75} nanoparticles and the many nanoscale interfaces that can scatter low to mid-frequency phonons because the low-frequency phonons can make an appreciable contribution to the thermal conductivity of the HMS samples and can have a mean free path comparable to the size and separation between ReSi_{1.75} nanoparticles.

To understand better the effect of Re substitution on the lattice thermal conductivity, the experimental result is compared with a calculation based on a model by Callaway et al. [49] At temperatures higher than the Debye temperature (θ_D), phonon grain boundary scattering may be ignored in polycrystalline materials with grain sizes larger than the phonon-phonon scattering mean free path. If only Umklapp scattering and point defect scattering are considered, the ratio of κ_L of the crystal with disorder to that without disorder (κ_{L0}) can be expressed as [8,50]

$$\frac{\kappa_{\rm L}}{\kappa_{\rm L0}} = \frac{\tan^{-1}(u)}{u}, u^2 = \frac{\pi^2 \theta_{\rm D} \Omega}{h v_{\rm a}^2} \kappa_{\rm L0} \Gamma, \tag{2}$$

where u, v_a , Ω , h, and Γ are the disorder scaling parameter, the average sound velocity, the average volume per atom, the Plank's constant, and the disorder scattering parameter, respectively. The disorder scattering parameter Γ can be calculated as $\Gamma_{\rm calc} = \Gamma_{\rm M} + \Gamma_{\rm S}$, where $\Gamma_{\rm M}$ and $\Gamma_{\rm S}$ are scattering parameters due to mass and strain-field fluctuations, respectively. For ${\rm Re_x Mn_{1-x}Si_{1.8}}$, $\Gamma_{\rm M}$ and $\Gamma_{\rm S}$ are given by [8,9]

$$\Gamma_{\rm M} = \frac{1}{2.8} \left(\frac{\overline{M}}{\overline{\overline{M}}}\right)^2 x (1 - x) \left(\frac{M_1 - M_2}{\overline{M}}\right)^2 \tag{3}$$

$$\Gamma_{\rm S} = \frac{1}{2.8} \left(\frac{\overline{M}}{\overline{\overline{M}}} \right)^2 x (1 - x) \varepsilon \left(\frac{r_1 - r_2}{\overline{r}} \right)^2 \tag{4}$$

$$\overline{M} = M_1 x + M_2 (1 - x) \tag{5}$$

$$\overline{\overline{M}} = \frac{1}{2.8}\overline{M} + \frac{1.8}{2.8}M_3 \tag{6}$$

and

$$\overline{r} = r_1 x + r_2 (1 - x) \tag{7}$$

Table 1. Density and room temperature physical properties of various $Re_xMn_{1-x}Si_{1.8}$ samples. The uncertainties of the measured transport properties are given in the caption of Figure 5.

Nominal composition	Density [g cm ⁻³]	σ [Ω^{-1} cm $^{-1}$]	S [μV K ⁻¹]	R _H [10 ⁻⁹ m ³ C ⁻¹]	p [10 ²¹ cm ⁻³]	$\mu_{\rm H}$ [cm ² V ⁻¹ s ⁻¹]	m*/m _o	E _F [eV]	L [10 ⁻⁸ V ² K ⁻²]
x = 0	4.87	475	122	4.05	1.54	1.92	9.6	0.81	1.54
<i>x</i> = 0.01	4.90	480	115	3.81	1.64	1.83	9.2	0.82	1.43
x = 0.02	4.95	524	114	3.69	1.70	1.93	9.4	0.82	1.35
x = 0.04	4.97	482	108	3.72	1.68	1.79	8.9	0.82	1.35
<i>x</i> = 0.06	4.98	430	106	3.56	1.76	1.53	8.8	0.83	1.50
x = 0.12	5.15	378	104	3.50	1.79	1.32	8.7	0.83	1.67

www.advenergymat.de

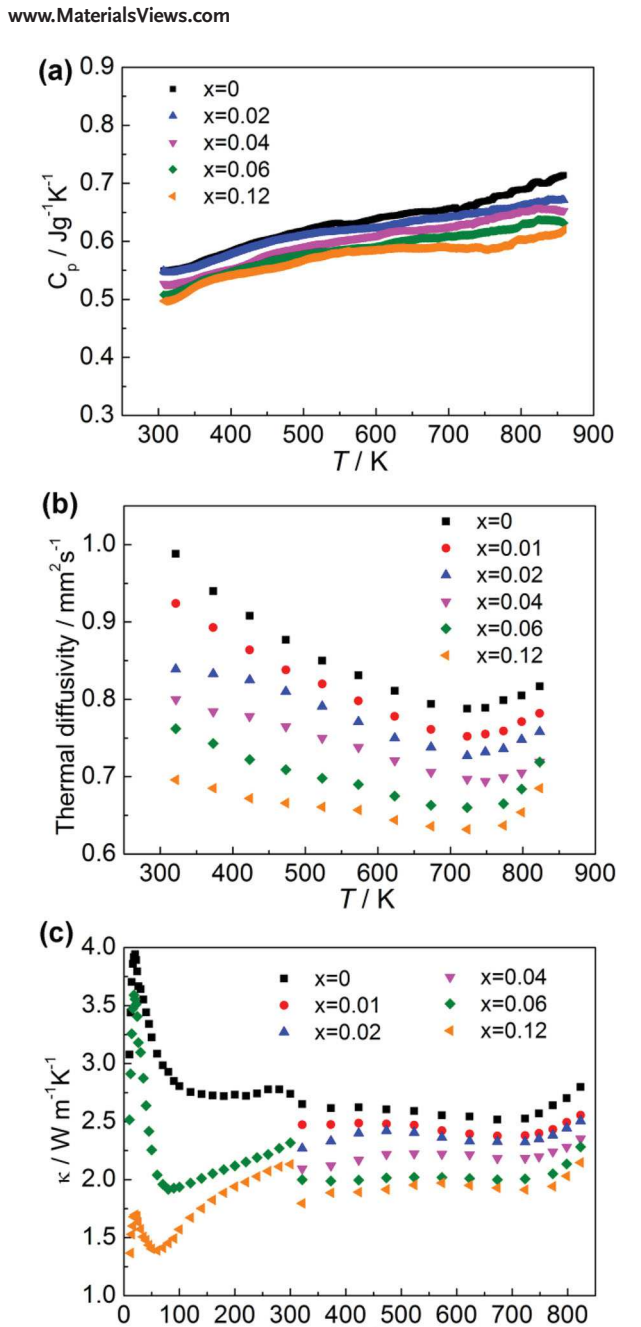
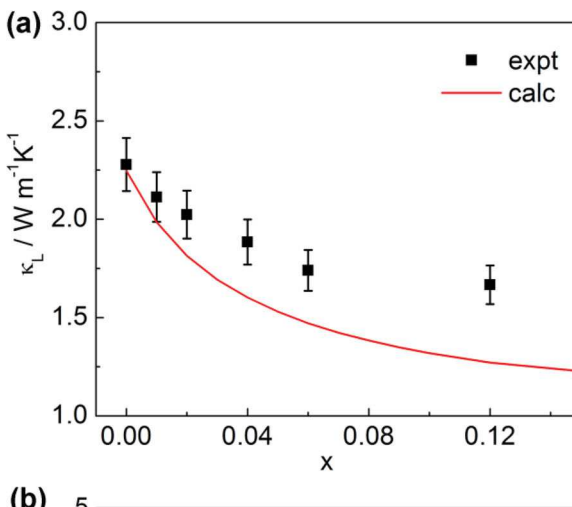


Figure 6. Temperature dependence of a) specific heat with 6% uncertainty, b) thermal diffusivity with 3% uncertainty, and c) total thermal conductivity, with 7% uncertainty for the laser flash method and 15% uncertainly for the steady-state method, of various $Re_xMn_{1-x}Si_{1.8}$ samples.

T/K

where M_1 , M_2 , and M_3 are the atomic mass values of Re, Mn, and Si, respectively, r_1 and r_2 are the atomic radius of Re and Mn, respectively, x is the Re content, and ε is a function of the Grüneisen parameter γ , as given below.

In order to determine the Debye temperature, the sound velocity and the parameter ε , the elastic properties of HMS were measured and listed in **Table 2**. The average sound velocity ν_a can be calculated from the measured longitudinal (ν_l) and shear (ν_s) sound velocities by^[51]



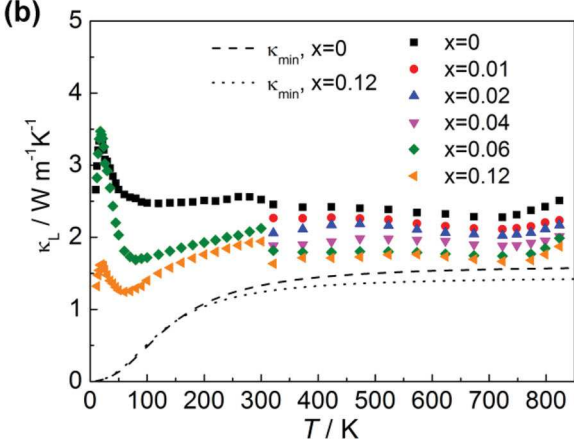


Figure 7. a) Lattice thermal conductivity of various $Re_xMn_{1-x}Si_{1.8}$ samples at 723 K as a function of x. The red line is the calculated lattice thermal conductivity based on the Callaway model. b) Temperature dependence of lattice thermal conductivity of $Re_xMn_{1-x}Si_{1.8}$. The dashed line and dotted lines are the calculated minimum lattice thermal conductivity of pure HMS and $Re_{0.12}Mn_{0.88}Si_{1.8}$, respectively.

$$\nu_{\rm a} = \left(\frac{1}{3} \left[\frac{1}{\nu_{\rm l}^3} + \frac{2}{\nu_{\rm s}^3} \right] \right)^{-1/3} \tag{8}$$

The Debye temperature θ_D can be obtained as:^[50]

$$\theta_{\rm D} = \frac{h}{k_{\rm B}} \left[\frac{3n}{4\pi} \right]^{1/3} \nu_{\rm a} \tag{9}$$

where n is the number density of atoms. The parameter ε is given by $[^{50]}$

$$\varepsilon = \frac{2}{9} \left(\frac{6.4\gamma (1 + \upsilon_p)}{(1 - \upsilon_p)} \right)^2 \tag{10}$$

where v_p is the Poisson ratio, and γ can be obtained from [52]

$$\gamma = \frac{3}{2} \left(\frac{1 + \nu_{\rm p}}{2 - 3\nu_{\rm p}} \right) \tag{11}$$

www.MaterialsViews.com

Table 2. Elastic properties of HMS at room temperature.

Parameters	Units	Value
Longitudinal sound velocity (ν_l)	$m s^{-1}$	7545
Shear sound velocity (ν_s)	${\rm m\ s^{-1}}$	4615
Average sound velocity (v_a)	${\rm m\ s^{-1}}$	5095
Young's modulus (E)	Gpa	245
Debye temperature ($\theta_{ m D}$)	K	660
Poisson ratio (v_p)	/	0.2
Grüneisen parameter (γ)	/	1.29

As listed in **Table 3**, $\Gamma_{\rm calc}$ increases with Re substitution. In addition, the calculated $\Gamma_{\rm M}$ is much larger than $\Gamma_{\rm S}$, suggesting that the mass fluctuation contribution dominates the contribution resulting from the strain-field fluctuation. Using the measured $\kappa_{\rm L}$ of pure HMS, which is $\kappa_{\rm L0} = 2.3$ W m⁻¹ K⁻¹, and $\Gamma_{\rm calc}$, the lattice thermal conductivity due to point defect scattering can be calculated from Equation (2). The calculated result (Figure 7a) indicates that the κ_L value at 723 K can be reduced to about 1.2 W m⁻¹ K⁻¹ when x = 0.18, which is about half of the value for pure HMS prepared with the synthesis method reported here. The experimental data follow the same trend as the model prediction, although the experimental data are somewhat higher than the calculated results. If the measured $\kappa_{\rm L}$ are used to extract u, the experimental Γ (Γ_{expt}) values can be estimated from Equation (2). The obtained Γ_{expt} is about a factor of two smaller than Γ_{calc} , as shown in Table 3. The discrepancy could be due to the Debye approximation used in this model, which is only valid when the temperature is much lower than $\theta_{\rm D}$. In addition, this model does not accurately account for the contribution of the optical phonon modes to the thermal conductivity, which can be important in the complex HMS structure at high temperatures. Nevertheless, the reduction of $\kappa_{\rm I}$ by Re substitution is confirmed by both experimental results and theoretical analysis.

We have further evaluated the minimum κ_L of HMS using the model of Cahill et al.[39]

$$\kappa_{\min} = \left(\frac{\pi}{6}\right)^{1/3} k_{\rm B} n^{2/3} \sum_{i} \nu_{i} \left(\frac{T}{\theta_{i}}\right)^{2} \int_{0}^{\theta_{i}/T} \frac{x^{3} e^{x}}{\left(e^{x} - 1\right)^{2}} dx$$
 (12)

where the summation is over two transverse and one longitudinal polarizations, the cutoff frequency θ_i is expressed as $\theta_i = \nu_i (h/k_B)(3n/4\pi)^{1/3}$, and ν_i is the sound velocity for

each polarization. This equation is developed based on the Einstein model to calculate the minimum lattice thermal conductivity of highly disordered solids, where thermal transport is characterized by random walk of energy between localized oscillators of varying frequencies and the dominant energy transport is between nearest neighbours. The model is also based on the Debye approximation of the phonon dispersion. Although this model relies on overly simplified assumptions of the relaxation process, it has obtained thermal conductivity values consistent with measurement results of amorphous materials.^[39]

With $\theta_D=660$ K and $\nu_a=5095$ m s⁻¹, the κ_{min} for pure HMS is calculated to be about 1.6 W m⁻¹ K⁻¹ above 700 K as shown in Figure 7b (dashed line). For Re_{0.12}Mn_{0.88}Si_{1.8}, we have evaluated θ_D as^[53]

$$\frac{\theta_{D}(\text{Re}_{0.12}\text{Mn}_{0.88}\text{Si}_{1.8})}{\theta_{D}(\text{MnSi}_{1.8})} = \left[\frac{(M_{2})^{3/2} + 1.8(M_{3})^{3/2}}{0.12(M_{1})^{3/2} + 0.88(M_{2})^{3/2} + 1.8(M_{3})^{3/2}}\right]^{1/3}$$
(13)

According to Equations (9) and (13), the θ_D and ν_a for Re_{0.12}Mn_{0.88}Si_{1.8} are calculated to be 593 K and 4578 m s⁻¹, respectively. Therefore, the $\kappa_{\rm min}$ for Re_{0.12}Mn_{0.88}Si_{1.8} yields about 1.4 W m⁻¹ K⁻¹ above 700 K as shown in Figure 7b (dotted line). This value is comparable to those of amorphous glass. Moreover, it is noted that the measured κ_L of Re_{0.12}Mn_{0.88}Si_{1.8} approaches the calculated $\kappa_{\rm min}$.

Finally, the figure of merit (ZT) of $Re_xMn_{1-x}Si_{1.8}$ is displayed in **Figure 8**. Re substitution suppresses the lattice thermal conductivity of HMS considerably and has relatively little influence on the power factor when the Re concentration is x = 0.04and smaller. The ZT value is improved to 0.57 \pm 0.08 at about 800 K for x = 0.04. This ZT value of the pure Re_xMn_{1-x}Si_{1.8} is ≈25% higher than that of pure HMS. The ZT value decreases with further increase of the Re content ($x \ge 0.06$) because of a reduction in the power factors. Because the primary role of Re substitution is to reduce the lattice thermal conductivity instead of optimizing the carrier concentration for enhanced power factor, the maximum power factor of Re_xMn_{1-x}Si_{1.8} is still lower than that of (Al,Ge)-doped HMS.[36] Since the hole concentration of $Re_{0.04}Mn_{0.96}Si_{1.8}$, 1.68×10^{21} cm⁻³, is lower than the optimized value found in (Al,Ge)-doped HMS, 1.8- 2.2×10^{21} cm⁻³, [36] further improvement in ZT in Re-substituted HMS may be possible via rational choice of impurity doping elements to optimize the carrier concentration of the $Re_xMn_{1-x}Si_{1.8}$ system.

Table 3. Calculated disorder parameter (u) and the scattering parameters of $Re_xMn_{1-x}Si_{1.8}$.

Nominal composition	и	$\Gamma_{ m expt}$	$\Gamma_{ m calc}$	$\Gamma_{ ext{ iny M}}$	$\Gamma_{ extsf{S}}$
x = 0.01	0.47	0.022	0.044	0.042	0.002
<i>x</i> = 0.02	0.59	0.034	0.084	0.081	0.003
<i>x</i> = 0.04	0.78	0.060	0.158	0.151	0.007
<i>x</i> = 0.06	1.05	0.108	0.222	0.212	0.010
x = 0.12	1.22	0.145	0.367	0.347	0.020



www.advenergymat.de

www.MaterialsViews.com

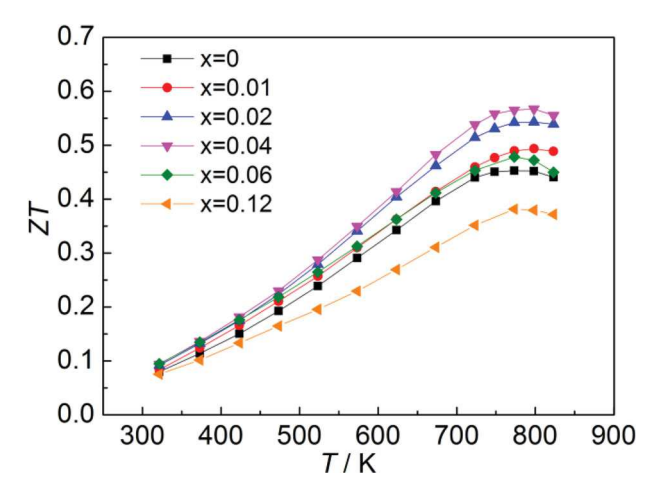


Figure 8. The dimensionless figure of merit (ZT) of various $Re_xMn_{1-x}Si_{1.8}$ samples with 13% uncertainty.

3. Conclusion

It is found in this experiment that the solubility limit of Re is about x = 0.18 in $Re_xMn_{1-x}Si_{1.8}$ that were synthesized by solid-state reaction followed by ball-milling and spark plasma sintering. Inhomogeneous distribution of Re and a secondary phase of ReSi_{1.75} nanoparticles were observed in the Re-substituted HMS samples. It is further observed that the electrical transport properties are modified by isoelectronic alloying of Re at Mn sites. With increasing Re content, the hole concentration increases slightly and the extracted effective hole mass and the mobility decrease. As a consequence, the power factor does not change significantly at low Re concentration of $x \le 0.04$, but it decreases with further increase of the Re content. The lattice thermal conductivity of Re-substituted HMS is considerably suppressed owing to enhanced alloy scattering, in agreement with the theoretical model. The κ_L value at x = 0.04and T = 723 K is suppressed to be about 1.8 W m⁻¹ K⁻¹, while the lowest κ_L is achieved in the sample with x = 0.12, which is about 1.6 W m⁻¹ K⁻¹ at 723 K. These values approach the calculated minimum $\kappa_{\rm I}$ value of 1.4 W m⁻¹ K⁻¹ for $T \ge 700$ K. Compared to pure HMS polycrystalline samples synthesized with the same method, the maximum ZT is increased by about 25% to 0.57 ± 0.08 at about 800 K in the sample with x = 0.04, which is due to a nearly unchanged power factor and a suppressed thermal conductivity. It is worth noting that the primary goal of Re substitution is to replace Mn with a heavier and isoelectronic element to reduce the lattice thermal conductivity, instead of serving as an impurity dopants to optimize the carrier concentration. Now that this goal has been achieved, the finding may enable further theoretical designs and experimental investigations of impurity doping strategies to optimize the carrier concentration and power factor of Re-substituted HMS.

4. Experimental Section

Synthesis: Re-substituted HMS, $Re_xMn_{1-x}Si_{1.8}$ (x=0-0.24), were synthesized by solid-state reaction (SSR) with subsequent ball milling (BM) and densification by spark plasma sintering (SPS). The starting materials, Mn (99.95%), Si (99.999%) and Re (99.99%) powders, were purchased from Alfa

Aesar. In a typical sample preparation, the powders with nominal chemical composition were sealed in a quartz tube under a vacuum of $\approx\!10^{-4}$ Torr. The quartz tube was placed in a furnace and sintered at 1173 K for 48 h. The as-sintered HMS powder was then loaded in a tungsten-carbide jar and ball milled for 60 min under argon in a SPEX 8000M Mixer/Mill (SPEX

SamplePrep). Subsequently, the ball-milled powders were consolidated into

dense bulk samples by SPS at 1123 K for 5 min under 60 MPa.

Phase Identification and Microstructure Characterization: The phase purity and crystal structure of the samples were studied by powder X-ray diffraction (PXRD) with a Phillip X'pert diffractometer with Cu K α radiation ($\lambda=1.54184$ Å). Several samples were ground to particle size <20 μm and analysed by high-resolution synchrotron PXRD at Argonne National Laboratory on the Advanced Photon Source (APS), beamline 11-BM, having a 12-analyzer Si detector and calibrated radiation wavelength of 0.412455 Å. The morphology and chemical compositions of finely-polished HMS samples were analysed with a Quanta 650 environmental SEM with an energy-dispersive X-ray (EDX) spectrometer. A Zeiss Crossbeam focused ion beam (FIB)/SEM was used to prepare samples that were analyzed by transmission electron microscopy (TEM) in a FEI Titan aberration-corrected (S)TEM electron microscope, operating at 200 kV.

Thermoelectric Transport Property Measurements: The electrical resistivity and Seebeck coefficient of samples with average dimensions of $1 \times 1 \times 6$ mm and $4 \times 4 \times 0.5$ mm, respectively, were measured in the temperature range of 10-823 K and 80-823 K, respectively, with homebuilt setups that have been independently calibrated. $^{[36]}$ The thermal diffusivity, α , was measured on disc-shaped samples with dimensions of $6 \times 6 \times 1$ mm by using the laser flash diffusivity method in a Netzsch LFA 457 instrument. The specific heat, C_p , was obtained with a Netzsch 404 differential scanning calorimeter (DSC) with a sapphire standard. The density, ρ , was measured by Archimedes' method. The total thermal conductivity in the range of 320 K to 850 K was calculated as $\kappa = \alpha C_{\rm p} \rho$. The thermal conductivity below 300 K was measured by a steady-state method on rectangular specimens (0.5 mm \times 0.5 mm \times 3 mm). All three transport properties were measured along the direction parallel to the SPS pressing direction. The room temperature Hall coefficient measurements were performed with a Physical Properties Measurement System (PPMS, Quantum Design) with the magnetic field sweeping between ±2 T. Because of the high carrier concentration of the degenerately doped HMS samples, the carrier concentration p and Hall mobility were calculated as $p = -(1/eR_H)$ and $\mu_H = \sigma R_H$, respectively, without accounting for the minority carriers. The sound velocities and elastic modulus were measured by resonant ultrasound spectroscopy at Oak Ridge National Laboratory (ORNL).

Acknowledgements

The work is supported by NSF/DOE Joint Thermoelectric Partnership (NSF award numbers: CBET-1048767 and CBET-1048625). S.N.G. gratefully acknowledges the NSF SEES Postdoctoral Fellowship for support (NSF award number EEC-1313968). The authors thank Dr. Matthew Suchomel at Argonne National Laboratory for help with high-resolution synchrotron PXRD measurement. Use of the Advanced Photon Source at Argonne National Laboratory was supported by the U. S. Department of Energy, Office of Science, Office of Basic Energy Sciences, under Contract No. DE-AC02-06CH11357. The SPS processing and Hall measurements at the University of Texas at Austin were conducted with instruments acquired with the support of NSF award number DMR-1229131 and DMR-1122603. The work at ORNL was supported by the Center for Revolutionary Materials for Solid State Energy Conversion, an Energy Frontier Research Center funded by the U.S. Department of Energy, Office of Science, Office of Basic Energy Sciences under Award Number DE-SC0001054.

> Received: March 14, 2014 Revised: April 10, 2014 Published online: May 21, 2014

www.MaterialsViews.com

- [25] A. J. Zhou, T. J. Zhu, X. B. Zhao, S. H. Yang, T. Dasgupta, C. Stiewe, R. Hassdorf, E. Mueller, J. Electron. Mater. 2010, 39, 2002.
- [26] V. Ponnambalam, D. T. Morelli, J. Electron. Mater. 2012, 41, 1389.
- [27] V. Ponnambalam, D. T. Morelli, S. Bhattacharya, T. M. Tritt, J. Alloy. Compd. 2013, 580, 598.
- [28] W. H. Luo, H. Li, F. Fu, W. Hao, X. F. Tang, J. Electron. Mater. 2011, 40, 1233.
- [29] Y. Kikuchi, Y. Miyazaki, Y. Saito, K. Hayashi, K. Yubuta, T. Kajitani, Jpn. J. Appl. Phys. 2012, 51, 085801.
- [30] N. L. Okamoto, T. Koyama, K. Kishida, K. Tanaka, H. Inui, Acta Mater. 2009, 57, 5036.
- [31] W. H. Luo, H. Li, Y. G. Yan, Z. B. Lin, X. F. Tang, Q. J. Zhang, C. Uher, *Intermetallics* 2011, 19, 404.
- [32] P. Norouzzadeh, Z. Zamanipour, J. S. Krasinski, D. Vashaee, J. Appl. Phys. 2012, 112, 124308.
- [33] T. Itoh, M. Yamada, J. Electron. Mater. 2009, 38, 925.
- [34] A. Pokhrel, Z. P. Degregorio, J. M. Higgins, S. N. Girard, S. Jin, Chem. Mater. 2013, 25, 632.
- [35] I. Aoyama, H. Kaibe, L. Rauscher, T. Kanda, M. Mukoujima, S. Sano, T. Tsuji, Jpn. J. Appl. Phys. Part 1 2005, 44, 4275.
- [36] X. Chen, A. Weathers, D. Salta, L. B. Zhang, J. S. Zhou, J. B. Goodenough, L. Shi, J. Appl. Phys. 2013, 114.
- [37] Y. Terazawa, M. Mikami, T. Itoh, T. Takeuchi, J. Electron. Mater. 2012, 41, 1348.
- [38] L. D. Ivanova, Inorg. Mater. 2011, 47, 965.
- [39] D. G. Cahill, S. K. Watson, R. O. Pohl, Phys. Rev. B 1992, 46, 6131.
- [40] A. J. Zhou, T. J. Zhu, X. B. Zhao, E. Mueller, J. Mater. Res. 2011, 26, 1900.
- [41] L. Pauling, The Nature of the Chemical Bond, 3rd ed, Cornell University Press, Ithaca, NY 1960, p. 403.
- [42] K. Kishida, A. Ishida, T. Koyama, S. Harada, N. L. Okamoto, K. Tanaka, H. Inui, Acta Mater. 2009, 57, 2010.
- [43] D. B. Migas, V. L. Shaposhnikov, A. B. Filonov, V. E. Borisenko, N. N. Dorozhkin, *Phys. Rev. B* **2008**, *77*, 075205.
- [44] A. Allam, P. Boulet, M.-C. Record, J. Electron. Mater. 2014, 43, 761.
- [45] G. A. Slack, M. A. Hussain, J. Appl. Phys. 1991, 70, 2694.
- [46] M. Glicksman, Phys. Rev. 1958, 111, 125.
- [47] J. Bardeen, W. Shockley, Phys. Rev. 1950, 80, 72.
- [48] I. Nishida, J. Mater. Sci. 1972, 7, 435.
- [49] J. Callaway, H. C. von Baeyer, Phys. Rev. 1960, 120, 1149.
- [50] Y. L. Pei, J. Q. He, J. F. Li, F. Li, Q. J. Liu, W. Pan, C. Barreteau, D. Berardan, N. Dragoe, L. D. Zhao, NPG Asia Mater. 2013, 5.
- [51] K. Kurosaki, A. Kosuga, H. Muta, M. Uno, S. Yamanaka, Appl. Phys. Lett. 2005. 87.
- [52] D. S. Sanditov, V. N. Belomestnykh, Tech. Phys. 2011, 56, 1619.
- [53] M. Bouvier, P. Lethuillier, D. Schmitt, Phys. Rev. B 1991, 43, 13137.

- [1] F. J. DiSalvo, Science 1999, 285, 703.
- [2] B. C. Sales, Science 2002, 295, 1248.
- [3] X. B. Zhao, X. H. Ji, Y. H. Zhang, T. J. Zhu, J. P. Tu, X. B. Zhang, Appl. Phys. Lett. 2005, 86, 062111.
- [4] B. Poudel, Q. Hao, Y. Ma, Y. C. Lan, A. Minnich, B. Yu, X. A. Yan, D. Z. Wang, A. Muto, D. Vashaee, X. Y. Chen, J. M. Liu, M. S. Dresselhaus, G. Chen, Z. F. Ren, *Science* 2008, 320, 634.
- [5] K. Biswas, J. Q. He, I. D. Blum, C. I. Wu, T. P. Hogan, D. N. Seidman, V. P. Dravid, M. G. Kanatzidis, *Nature* 2012, 489, 414
- [6] J. R. Szczech, J. M. Higgins, S. Jin, J. Mater. Chem. 2011, 21, 4037.
- [7] Z.-Y. Li, J.-F. Li, Adv. Energy Mater. 2014, 4, 1300937.
- [8] J. Yang, G. P. Meisner, L. Chen, Appl. Phys. Lett. 2004, 85, 1140.
- [9] C. G. Fu, H. H. Xie, T. J. Zhu, J. Xie, X. B. Zhao, J. Appl. Phys. 2012, 112.
- [10] X. Y. Shi, Y. Z. Pei, G. J. Snyder, L. D. Chen, Energy Environ. Sci. 2011, 4 4086
- [11] W. Liu, X. F. Tang, H. Li, K. Yin, J. Sharp, X. Y. Zhou, C. Uher, J. Mater. Chem. 2012, 22, 13653.
- [12] Y. Pei, A. F. May, G. J. Snyder, Adv. Energy Mater. 2011, 1, 291.
- [13] J. P. Heremans, V. Jovovic, E. S. Toberer, A. Saramat, K. Kurosaki, A. Charoenphakdee, S. Yamanaka, G. J. Snyder, *Science* 2008, 321,
- [14] W. Liu, X. Tan, K. Yin, H. Liu, X. Tang, J. Shi, Q. Zhang, C. Uher, Phys. Rev. Lett. 2012, 108.
- [15] Y. Pei, X. Shi, A. LaLonde, H. Wang, L. Chen, G. J. Snyder, *Nature* 2011, 473, 66.
- [16] H. Liu, X. Shi, F. Xu, L. Zhang, W. Zhang, L. Chen, Q. Li, C. Uher, T. Day, G. J. Snyder, *Nat. Mater.* 2012, 11, 422.
- [17] S. K. Bux, A. Zevalkink, O. Janka, D. Uhl, S. Kauzlarich, J. G. Snyder, J. P. Fleurial, J. Mater. Chem. A 2014, 2, 215.
- [18] O. G. Karpinski, B. A. Evseev, Izv. Akad. Nauk SSSR, Neorg. Mater. 1969, 5, 525.
- [19] O. Schwomma, A. Preisinger, H. Nowotny, A. Wittmann, *Monatsh. Chem. Verw. TL.* **1964**, *95*, 1527.
- [20] H. W. Knott, M. H. Mueller, L. Heaton, Acta Crystallogr. 1967, 23, 549.
- [21] J. M. Higgins, A. L. Schmitt, I. A. Guzei, S. Jin, J. Am. Chem. Soc. 2008, 130, 16086.
- [22] G. Zwilling, H. Nowotny, Monatsh. Chem. 1971, 102, 672.
- [23] M. I. Fedorov, V. K. Zaitsev, in Thermoelectric Handbook: Macro to Nano, (Ed: D. M. Rowe), CRC/Taylor & Francis, Boca Raton, FL 2006. p. 36.
- [24] I. Aoyama, M. I. Fedorov, V. K. Zaitsev, F. Y. Solomkin, I. S. Eremin, A. Y. Samunin, M. Mukoujima, S. Sano, T. Tsuji, Jpn. J. Appl. Phys. 2005, 44, 8562.